Check for updates

Transverse phase matching of high-order harmonic generation in single-layer graphene

ROBERTO BOYERO-GARCÍA,* OSCAR ZURRÓN-CIFUENTES, LUIS PLAJA, AND CARLOS HERNÁNDEZ-GARCÍA

Grupo de Investigación en Aplicaciones del Láser y Fotónica, Departamento de Física Aplicada, Universidad de Salamanca, E- 37008 Salamanca, Spain
*robertobg@usal.es

Abstract: The efficiency of high-harmonic generation (HHG) from a macroscopic sample is strongly linked to the proper phase matching of the contributions from the microscopic emitters. We develop a combined micro+macroscopic theoretical model that allows us to distinguish the relevance of high-order harmonic phase matching in single-layer graphene. For a Gaussian driving beam, our simulations show that the relevant HHG emission is spatially constrained to a phase-matched ring around the beam axis. This remarkable finding is a direct consequence of the non-perturbative behavior of HHG in graphene—whose harmonic efficiency scaling is similar to that already observed in gases— and bridges the gap between the microscopic and macroscopic HHG in single-layer graphene.

1. Introduction

Since its discovery in the late 80s [1,2], high-harmonic generation (HHG) has turned out to be a remarkably rich process in nonlinear optics. The interaction of intense femtosecond laser pulses with an atomic, molecular, or solid target drives electrons to a non-perturbative dynamics, resulting in the generation of coherent high-frequency radiation, extending from extreme ultraviolet to soft x-rays [3]. High-frequency harmonics are emitted in the form of ultrashort pulses, with temporal durations at the attosecond timescale [4,5].

While the vast majority of studies and applications of HHG have been developed in the context of atomic and molecular targets, its demonstration in solids targets [6] has boosted a considerable interest in the recent years. In atoms and molecules, HHG is well understood in semiclassical terms [7]: an electronic wavepacket is ejected from its parent atom through tunnel ionization driven by the laser field. Once in the continuum, the electron is accelerated by the field. Upon reversal of the field amplitude, the electron is driven back to the ion, where it recollides, releasing its kinetic energy as high-frequency harmonics of the driving field. HHG in solid systems follows similar physical mechanisms [8,9]. For the case of finite-gap solids, ionization is replaced by tunnel excitation from the valence to the conduction band, and interband harmonics are radiated upon electron-hole recombination [9]. Up to now, HHG has been observed in different finite-gap solids, such as ZnO, MoS_2, ZnSe, GaSe or SiO_2 [6,10–14]. Low-dimensional systems, as single-layer graphene, have also been recently demonstrated to produce high-order harmonics [15] where, interestingly, tunnel excitation is replaced by an electron-hole pair creation from the non-adiabatic crossings near the Dirac points [16]. Such mechanism leads to the emission of a complex set of electron-hole trajectories responsible for HHG [16–18], very different to those in bulk solids [19]. In addition to the interband contributions, solid systems also present HHG from intraband dynamics [9]. Nowadays many theoretical works have explored HHG in solids at the microscopic level to gain understanding into these dynamics [9,16,20–25], probing that HHG can serve as a unique spectroscopic tool to unveil the structural dynamics of solid materials [13,14].

One of the potential advantages of HHG from solids is the capability to produce brighter harmonics, due to the larger number of emitters involved. The efficiency of the macroscopic

harmonic emission, however, depends crucially on the phase matching of the microscopic contributions. Phase matching in HHG has been extensively studied in atoms and molecules [26–33], and several theoretical methods have been proposed [34–43]. There are many examples where the emitted harmonic radiation is controlled tuning only macroscopic parameters, such as the isolation of attosecond pulses [44,45], the generation of circularly polarized harmonics [46,47], lenless focusing of high-order harmonics [48,49], or the generation of structured harmonics with custom orbital angular momentum or self-torque properties [50–52], among others. However, up to now few works have theoretically studied the macroscopic picture of HHG in solids. Floss and coworkers [53] coupled ab-initio simulations of the time-dependent density functional theory with the Maxwell equations to study macroscopic effects of HHG in diamond along the propagation direction. The primary effect observed in the macroscopic signal was the production of a cleaner harmonic spectra, an effect that is universally observed in experiments, and which has been previously invoked phenomenologically in theoretical simulations by including short dephasing times [9,13,24]. Moreover, macroscopic HHG in Dirac-Weyl materials such as single-layer graphene, where excitation takes place through the Dirac points, remains unstudied.

One could think that microscopic HHG is a reasonable approximation to the target emission for single-layer graphene, as the propagation length is at the atomic scale. However, HHG is a non-perturbative process and, therefore, the harmonic emission depends strongly on the driving field's intensity. In particular, the harmonic phase of the microscopic emission is substantially affected by the driver's intensity profile. Therefore, in the non-perturbative case, the concept of harmonic phase matching, and the associated coherence length, must be extended to describe also phase differences in the plane transverse to propagation [54]. It has been demonstrated that transverse phase matching in atomic gases plays a relevant role to enhance the HHG efficiency [54], and to shape the temporal [55] or spatial properties [48,49,56] of the high-order harmonics—specially for structured driving fields—, as it is the case when they carry orbital angular momentum [50]. Transverse phase matching should be thus expected to be of paramount importance in HHG in low-dimensional solids, for orthogonal driver incidences, where longitudinal propagation distances are reduced to the atomic size.

In this work we develop theoretical simulations of macroscopic HHG in single-layer graphene, that combine the numerical integration of the time-dependent Schrödinger equation and the electromagnetic field propagator. Our simulations demonstrate that phase matching plays a relevant role in the macroscopic spectrum, despite the two-dimensional nature of graphene. As a main result, we demonstrate that macroscopic HHG in single-layer graphene irradiated by a Gaussian driving beam is effectively confined to a phase-matched ring. This spatial confinement follows from the non-perturbative scaling law of the harmonic efficiencies with the driver intensity, thus being a particular feature of HHG, not found in other photon conversion processes. We thus establish a fundamental connection between the non-perturbative strong-field physics at the microscopic level and the macroscopic HHG in single-layer graphene. Our numerical method and our results pave the route for the complete theoretical study of HHG in other solid systems—such as Dirac-Weyl materials—, or in other configurations—such as the use of structured driving beams—that require the description of the macroscopic picture.

2. Microscopic vs macroscopic HHG in single-layer graphene

2.1. Theoretical method: time-dependent Schrödinger equation coupled with the electromagnetic field propagator

Our method integrates both the microscopic and macroscopic description of HHG in single-layer graphene. The calculations at the microscopic level combine the tight-binding description of the valence and conduction bands in graphene with the solution of the time-dependent Schrödinger equation, as depicted in [16].

We consider a nearest-neighbor tight-binding model to describe the electron dynamics in the periodic potential of graphene. The energy spectrum of the field-free hamiltonian, H_0, consists of two bands, the conduction band (+) and the valence band (-), with energy dispersion $\epsilon_{\pm}(\mathbf{k}) = \pm\gamma|f(\mathbf{k})|$ ($\gamma = 2.97$ eV) in the Brillouin zone, see Figs. 1(a) and (b), with

$$f(\mathbf{k}) = e^{-iak_x/\sqrt{3}}\left(1 + 2e^{i\sqrt{3}ak_x/2}\cos\frac{ak_y}{2}\right), \tag{1}$$

where $a = 2.45$. The Bloch-state wavefunctions can be expressed as:

$$\Phi_{\mathbf{k}}^{\pm}(\mathbf{r}) = \sqrt{\frac{1}{2}}e^{i\mathbf{k}\cdot\mathbf{r}}\begin{pmatrix} \pm 1 \\ e^{-i\phi(\mathbf{k})} \end{pmatrix}, \tag{2}$$

where $\phi(\mathbf{k})$ is the argument of the complex function $f(\mathbf{k})$. The time-dependent wave function can then be expressed as a superposition of the eigenstates described by Eq. (2):

$$\Psi(\mathbf{r}, t) = \int \Psi_{\mathbf{k}}(\mathbf{r}, t)d\mathbf{k} = \int \left[C_+(\mathbf{k}, t)\Phi_{\mathbf{k}}^+(\mathbf{r}) + C_-(\mathbf{k}, t)\Phi_{\mathbf{k}}^-(\mathbf{r}) \right] d\mathbf{k}. \tag{3}$$
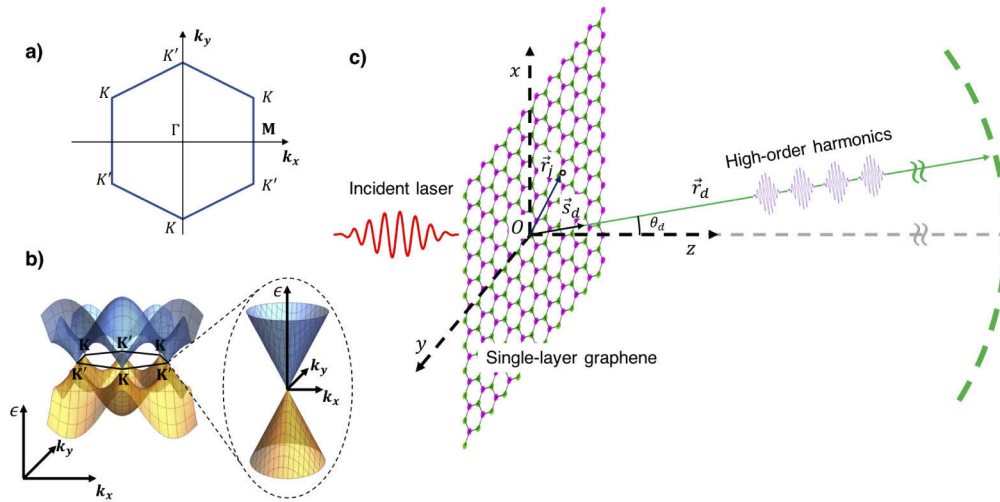

Fig. 1. Scheme of the micro+macroscopic HHG method to compute HHG in single-layer graphene. a) Scheme of graphene's first Brillouin Zone in the reciprocal space. b) Graphene's band structure within the nearest-neighbor tight-binding approximation. The Fermi level is set to zero. The conduction and valence bands correspond to positive and negative values of energy, respectively. Dirac points K and K' are degenerated in energy at the Fermi level. c) Interaction geometry considered. The driving field propagates along the z-direction, perpendicularly to the graphene layer, where high-order harmonics are generated. Afterwards, the high-order harmonics are propagated to a far-field detector placed at position $\mathbf{r}_d$ from the center of the layer (dashed green line).

The interaction of the driving laser pulse $\mathbf{E}(t)$ is described by the time-dependent Hamiltonian $H(t) = H_0 + V_i(t)$ and $V_i(t) = -q_e\mathbf{E}(t) \cdot \mathbf{r}$ is the coupling with the electric field, in the dipole approximation, q_e being the electron charge. We consider a driving field linearly polarized and aimed perpendicularly to the graphene layer, therefore the vector field $\mathbf{E}(t)$ is included in the graphene plane. If the duration of the pulse is less than the characteristic carrier scattering time

~ 10-100 fs [57–59], the electron dynamics can be described by the time-dependent Schrödinger equation [16]:

$$i\hbar\frac{d}{dt}C_+(\boldsymbol{\kappa}_t,t) = [\epsilon_+(\boldsymbol{\kappa}_t) - \mathbf{E}(t) \cdot \mathbf{D}(\boldsymbol{\kappa}_t)]\, C_+(\boldsymbol{\kappa}_t,t) - \mathbf{E}(t) \cdot \mathbf{D}(\boldsymbol{\kappa}_t)C_-(\boldsymbol{\kappa}_t,t), \tag{4}$$

$$i\hbar\frac{d}{dt}C_-(\boldsymbol{\kappa}_t,t) = [\epsilon_-(\boldsymbol{\kappa}_t) - \mathbf{E}(t) \cdot \mathbf{D}(\boldsymbol{\kappa}_t)]\, C_-(\boldsymbol{\kappa}_t,t) - \mathbf{E}(t) \cdot \mathbf{D}(\boldsymbol{\kappa}_t)C_+(\boldsymbol{\kappa}_t,t), \tag{5}$$

where $\hbar\boldsymbol{\kappa}_t = \hbar\mathbf{k} - q_e\mathbf{A}(t)/c$, being $\mathbf{A}(t)$ the vector potential and c the speed of light, and $\mathbf{D}(\mathbf{k}) = (q_e/2)\partial\phi/\partial\mathbf{k}$ is the interband matrix element , proportional to the Berry connection. We assume all states of the valence band occupied and all states of the conduction band empty before the interaction with the driving pulse, so we take $C_-(\mathbf{k},0) = 1$ and $C_+(\mathbf{k},0) = 0$ as initial conditions. The harmonic emission is then computed from the total dipole acceleration, $\mathbf{a}(t) = \frac{d^2}{dt^2}\mathbf{d}(t)$, with [16]

$$\mathbf{d}(t) = \langle\Psi|q_e\mathbf{r}|\Psi\rangle = iq_e\left[C_+^*(\boldsymbol{\kappa}_t,t)\nabla_{\boldsymbol{\kappa}_t}C_+(\boldsymbol{\kappa}_t,t) + C_-^*(\boldsymbol{\kappa}_t,t)\nabla_{\boldsymbol{\kappa}_t}C_-(\boldsymbol{\kappa}_t,t)\right] + $$
$$\mathbf{D}(\boldsymbol{\kappa}_t)\left[C_-^*(\boldsymbol{\kappa}_t,t)C_+(\boldsymbol{\kappa}_t,t) + C_-(\boldsymbol{\kappa}_t,t)C_+^*(\boldsymbol{\kappa}_t,t)\right]. \tag{6}$$

The intraband contribution to the total acceleration is computed as

$$\mathbf{a}_{\leftrightarrow}(t) = \frac{q_e^2}{\hbar^2}\mathbf{E}(t)\int\left[|C_+(\boldsymbol{\kappa}_t,t)|^2\frac{\partial^2\epsilon_+(\boldsymbol{\kappa}_t)}{\partial\mathbf{k}^2} + |C_-(\boldsymbol{\kappa}_t,t)|^2\frac{\partial^2\epsilon_-(\boldsymbol{\kappa}_t)}{\partial\mathbf{k}^2}\right]d\mathbf{k}. \tag{7}$$

In order to take into account macroscopic effects of HHG, one should solve the wave equation for the electric field $\mathbf{E}$,

$$\nabla^2\mathbf{E} - \frac{1}{c^2}\frac{\partial^2}{\partial t^2}\mathbf{E} = \frac{4\pi}{c^2}\frac{\partial}{\partial t}\mathbf{J}, \tag{8}$$

where $\mathbf{J}$ is the current density. We will adopt a similar strategy as in [41], whose results have been validated with experiments in HHG in atomic and molecular gases (as for example in Refs. [3,44,46,47,51,52,54,55,60]). We consider, therefore, the formal integral solution: $\mathbf{E}(\mathbf{r},t) = \mathbf{E}_0(\mathbf{r},t) + \mathbf{E}_i(\mathbf{r},t)$, where $\mathbf{E}_0(\mathbf{r},t)$ is the laser field, as it propagates in vacuum, and $\mathbf{E}_i(\mathbf{r},t)$ is the field radiated by the accelerated charges in the target,

$$\mathbf{E}_i(\mathbf{r},t) = -\frac{1}{c^2}\int d\mathbf{r}'\frac{1}{|\mathbf{r}-\mathbf{r}'|}\left[\frac{\partial}{\partial t'}\mathbf{J}(\mathbf{r}',t')\right]_{t'=t-|\mathbf{r}-\mathbf{r}'|/c}. \tag{9}$$

The far field radiated by the jth charge in the layer, reaching the detector placed at $\mathbf{r}_d$ (see Fig. 1(c)), can be written as,

$$\mathbf{E}_i^j(\mathbf{r}_d,t) = \frac{1}{c^2}\frac{q_j}{|\mathbf{r}_d - \mathbf{r}_j(0)|}\mathbf{s}_d \times \left[\mathbf{s}_d \times \mathbf{a}_j(t - |\mathbf{r}_d - \mathbf{r}_j(0)|/c)\right], \tag{10}$$

where $\mathbf{a}_j$ is the charge's acceleration, evaluated at the retarded time, and $\mathbf{s}_d$ is the unitary vector pointing towards the detector. We discretize the layer into a random distribution of spatial regions of size much smaller that the driver's wavelength, where the driving field can be assumed homogeneous. These elemental regions, however, still include a number of graphene primitive cells large enough to approximate the Brillouin zone to a continuum. Therefore, the macroscopic signal radiated by the graphene layer can be written as the superposition of the individual contributions $\mathbf{E}_i(\mathbf{r},t) = \sum_{j=1}^{N}\mathbf{E}_i^j(\mathbf{r},t)$, corresponding to each of the regions. The number of elemental regions considered must be large enough to ensure convergence of the radiation at the detector. Note that for a two-dimensional target, Eq. (9) corresponds to the Huygens-Fresnel diffraction formula.

2.2. Microscopic vs macroscopic results

We consider as driving field a linearly polarized 3 μm-wavelength Gaussian beam of 30 μm beam waist, aimed perpendicularly to the graphene layer, with a peak intensity of 3.5×10^{12} W/cm^2, well below the threshold damage of graphene [61]. The driving field is modelled with a sin^2 envelope of 8 cycles temporal length—corresponding to 28.8 fs full width at half maximum (FWHM)—smaller than the decoherence time due to carrier collisions [57–59].

The microscopic HHG spectrum corresponding to the driving field at the beam center, and obtained from Eq. (6), is shown in Fig. 2(a) (blue line). It presents a non-perturbative plateau of harmonics extending towards a cutoff frequency. As commented before, the generation of this high-frequency radiation is understood in terms of interband and intraband transitions. The contribution of the intraband transitions, calculated from Eq. (7), is shown in the cyan line. It can be concluded, therefore, that interband transitions are the main responsible for the generation of the high-frequency harmonics. As studied in [16], interband HHG is produced by electron-hole pairs created during the non-adiabatic crossings near the Dirac points, followed by their recombination at the emission time. The electron-hole pair can follow complex trajectories before recombining, which gives rise to unstructured spectra.

We have computed the macroscopic response considering the graphene layer at the focus of the Gaussian beam, where the driving field exhibits a transverse intensity profile with uniform phase. The on-axis detected coherent superposition of the microscopic contributions introduced in Section 2.1 is presented in filled-red in Fig. 2(a). In order to highlight the role of phase matching, we also include in the figure the spectrum corresponding to the incoherent addition of the microscopic fields (black line), where the harmonic phase is artificially ignored when obtaining the far-field emission. The coherent addition cleans the spectrum, showing clearly visible harmonic peaks, an effect that has been also observed theoretically in diamond [53], and is universally observed in experiments of HHG in solids [6,10–12]. The coherent addition results also in a weaker harmonic signal compared with the incoherent addition, through all the HHG spectrum, thus demonstrating partial destructive interference due to phase mismatch. Also, the signal at odd harmonic frequencies shows much higher degree of coherence than that of the non-harmonic frequencies. To further show the cleaning of the HHG spectrum obtained when considering transverse phase-matching, we present in Figs. 2(b) and 2(c) the time-frequency analysis for the macroscopic (coherent addition) and microscopic cases, respectively. Though the family of trajectory contributions to HHG in graphene is very complex [16,18], the temporal emission is substantially cleaned when considering the macroscopic result (Fig. 2(c)). The comparison between microscopic and macroscopic cases demonstrates the relevance of considering phase matching in single-layer graphene to reproduce the harmonic signal detected in an experiment.

In addition, the intraband contribution to the coherent macroscopic response is shown in dark red in Fig. 2. Similarly to the microscopic response, the macroscopic response of the high-order harmonics is dominated by the interband transitions.

For the sake of completeness we show in Figs. 2(d) and 2(e) the far-field spatial distribution of the HHG spectrum corresponding to the coherent and incoherent macroscopic additions, respectively. Note that the profiles at zero divergence correspond to the HHG spectra shown in filled-red and black in Fig. 2(a), respectively. The comparison between the spatial profiles reveals that the coherent macroscopic addition results in a much narrower emission of the HHG radiation. In addition, the coherent macroscopic harmonics exhibit a divergence that decreases with the harmonic order, a direct consequence of the non-perturbative behavior of HHG in graphene, as we demonstrate in the next section.
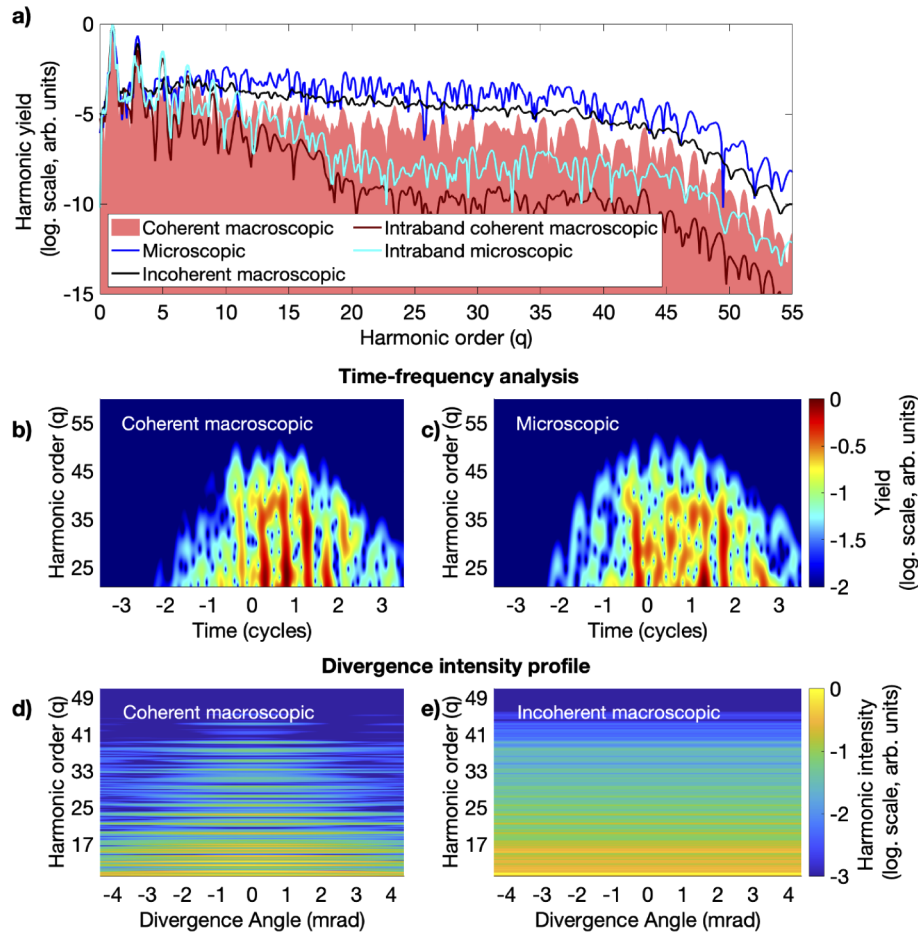
Fig. 2. (a) Comparison between the microscopic and macroscopic HHG spectrum in single-layer graphene irradiated by a 3 μm in wavelength, 28.8 fs FWHM, and 3.5×10^{12} W/cm^2 peak intensity Gaussian beam (30 μm beam waist). The microscopic spectrum obtained at the center of the Gaussian profile is shown as a blue line, the macroscopic HHG spectrum resulting from the coherent (incoherent) addition of the microscopic contributions are shown in filled-red (black line). The spectrum in the microscopic case has been rescaled to the peak at the fundamental frequency of the macroscopic coherent addition. The intraband contributions are shown in solids lines for the microscopic (cyan) and coherent macroscopic (dark red) cases. Time-frequency analysis (log. scale) of the (b) coherent macroscopic and (c) microscopic harmonic emission, performed with a spectral Gaussian mask of width $3\omega_0$, where ω_0 is the frequency of the driving laser pulse. The far-field intensity divergence profile is shown in panels (d) and (e) for the coherent and incoherent macroscopic additions, respectively.

3. Phase-matched ring and atom-like features in non-perturbative harmonic generation from graphene

In order to gain insight into the build-up of the the macroscopic harmonic signal presented in Fig. 2, we now analyze the high-order emission at different positions along the graphene layer. The qth-order harmonic far-field emission detected on-axis can be found from the Fraunhofer integral

$$U'_q = \frac{2\pi e^{ikz}}{iz\lambda_q} \int U_q(\rho)\rho d\rho, \tag{11}$$

where $U_q(\rho)$ is the microscopic harmonic field emitted at each point of the graphene slab, proportional to the dipole acceleration, Eq. (6). $U_q(\rho)$ inherits the cylindrical symmetry from the driving field, a Gaussian beam. We present in Fig. 3 the contributions of the different radii in Eq. (11), $U_q(\rho)\rho$, in amplitude and phase, i.e., the near-field harmonic emission weighted by the distance to the beam center. Remarkably, Fig. 3(a) shows that the most prominent high harmonic field amplitudes (orders above the 13th in the figure) are radiated from a limited, annular, region around a radius that we denote as ρ_{max}. However, the overall efficiency of this ring depends crucially on the degree of phase matching around it. We plot, therefore, in Fig. 3(b) the phase distribution of $U_q(\rho)$ at the sample. Note that, for the higher-order harmonics, the phase variation shows two distinct regions, slower for smaller radii and faster for larger radii. Interestingly enough, the region enclosed by the ring of maximal amplitudes, ρ_{max}, belongs to the former one, ensuring a smooth variation of the phase and, therefore a proper phase matching condition.
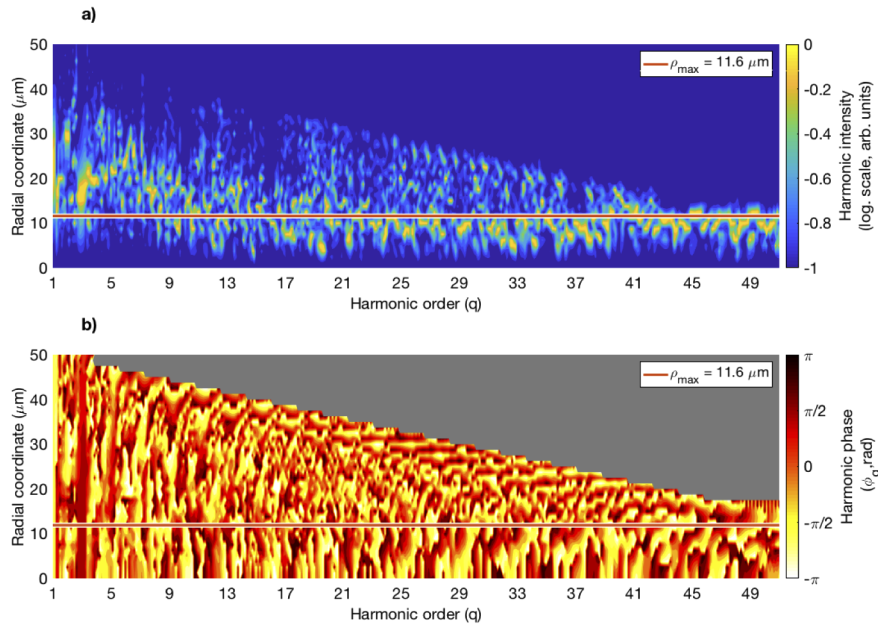

Fig. 3. (a) Harmonic intensity contribution $I_q(\rho)\rho$, and (b) harmonic phase, $\phi_q(\rho)$, of each spatial ring at the graphene layer, considering a Gaussian driving beam profile with beam waist $w_0 = 30$ μm. The harmonic intensity and phase are given by the Fourier transform of Eq. (6) for the same driving pulse parameters as in Fig. 2. The orange solid line indicates the position of the radius of maximum harmonic intensity contribution, $\rho_{max} = w_0/\sqrt{2p} = 11.6$ μm.

The presence of a phase-matched ring of similar radius for the high-harmonic orders is, in fact, a consequence of the non-perturbative character of the HHG process. To evidence this, we

will first demonstrate that microscopic HHG follows the same basic non-perturbative features in graphene as in gases. This is a surprising fact since, as mentioned before, the underlying mechanism of HHG in graphene differs in fundamental aspects from that in atoms. On one hand, the electron-hole pair creation is connected with the adiabatic crossing in the Dirac points, instead of tunnelling . On the other hand, harmonics are typically generated by a much more complex set of electron-hole trajectories. Nevertheless, we next see that the amplitude of the harmonics generated at the graphene target can still be approximated using a description valid for atoms [62],

$$U_q(\rho) \propto |U_0(\rho)|^p \, e^{i\left[q\phi_0(\rho)+\varphi_q(\rho)\right]}, \tag{12}$$

where q is the harmonic order, $U_0(\rho)e^{i\phi_0(\rho)}$ is the driving field amplitude, $\varphi_q(\rho)$ is the non-perturbative intrinsic phase, and $p<q$ is the power-scaling factor between the harmonic and the driver intensity, for harmonics in the plateau region. In the perturbative case, a similar relation would hold, but with the absence of the intrinsic phase and replacing the scaling factor p by the harmonic order q. Therefore, the non-perturbative nature of HHG is connected with a constant scaling exponent, p, and the additional intrinsic term in the phase.

In order to estimate the behaviour of the power scaling in graphene, we present in Fig. 4(a) the intensity scaling of different harmonic orders (the 19th, 29th and 39th) with the driving field intensity. The logarithmic fit represented in solid lines in Fig. 4(a) allows us to extract the power scaling p, being 2.0, 3.4 and 3.6 for the 19th, 29th and 39th harmonics respectively. In Fig. 4(b) we show the extracted power scaling as a function of the harmonic order for three different driving intensities: 1.3×10^{12} W/cm^2 (dashed red), 3.5×10^{12} W/cm^2 (solid black, same as that used in Fig. 2(a)), and 6.9×10^{12} W/cm^2 (dashed blue). The grey solid line indicates the perturbative power scale behaviour $p = q$. From the results presented in Fig. 4 we can clearly conclude that in HHG in graphene the power scaling is clearly non-perturbative, $p<q$, lying between 2 and 4 in the plateau region, close to the values reported for HHG in atomic gases [49,50,62,63].

Now we can estimate the position of the radius of maximum harmonic contribution, , introduced in Fig. 3. Inserting Eq. (12) in Eq. (11), assuming a Gaussian profile for the driving field at the target with waist w_0, $U_0(\rho) = U_0 e^{-\frac{\rho^2}{w_0^2}}$, and using Eq. (12), the radius of the ring with maximal contribution to the integral Eq. (11) can be found as

$$\frac{\partial \left(U_0^p e^{-p\frac{\rho^2}{w_0^2}} \rho \right)}{\partial \rho} = 0 \longrightarrow \rho_{\max} = \frac{w_0}{\sqrt{2p}}. \tag{13}$$

Note that in the perturbative case ($p = q$) the radii would depend on the harmonic order. In the non-perturbative case, however, p is constant and the high harmonics will be preferentially emitted from the same annular region in the target. For the case shown in Fig. 3, the red line corresponds to ρ_{max} =11.6 μm for p =3.3.

The final HHG efficiency depends on the width of the annular region around ρ_{max} for which the microscopic emissions are properly phase-matched. We show in Fig. 5 the relative phase of the harmonic emission near the ring of maximum efficiency, $\phi_q(\rho) - \phi_q(\rho_{max})$, for the case shown in Fig. 2(a). Note that we only show the phase values at the harmonic peaks, considering as a reference the coherent addition (filled-red line) of Fig. 2(a). The green lines indicate the radii for which the harmonic phase difference is $\pm\pi/2$, relative to the emission at $\rho = \rho_{\max}$, i.e. where the harmonic emission can be considered phase-matched.

The analysis of the intensity and phase profiles in Figs. 3 and 5 allows us to identify the width of the phase-matched graphene ring. The relevance of this ring to the total harmonic emission is illustrated in Fig. 6(a), where we show the HHG emission resulting from the whole graphene layer (filled-red, same as that in Fig. 2(a)), and from rings centered at $\rho = \rho_{\max}$ with thicknesses
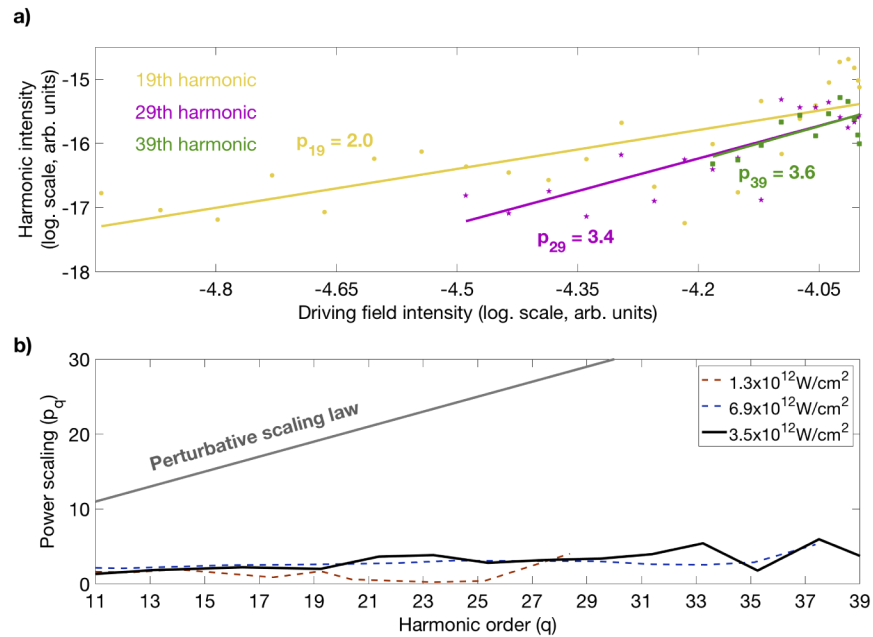
Fig. 4. (a) Intensity scaling of the 19th (yellow), 29th (pink), and 39th (green) harmonics with the driving field intensity (log. scale), obtained through the microscopic calculation of HHG in single-layer graphene. The solid lines indicate the fit for extracting the power scaling p_q. (b) Power scaling p_q as a function of the harmonic order for 1.3×10^{12} W/cm^2 (dashed red), 3.5×10^{12} W/cm^2 (solid black, same intensity as in Fig. 2), and 6.9×10^{12} W/cm^2 (dashed blue) driving intensities. The grey solid line indicates the perturbative power scale behaviour $p_q = q$.
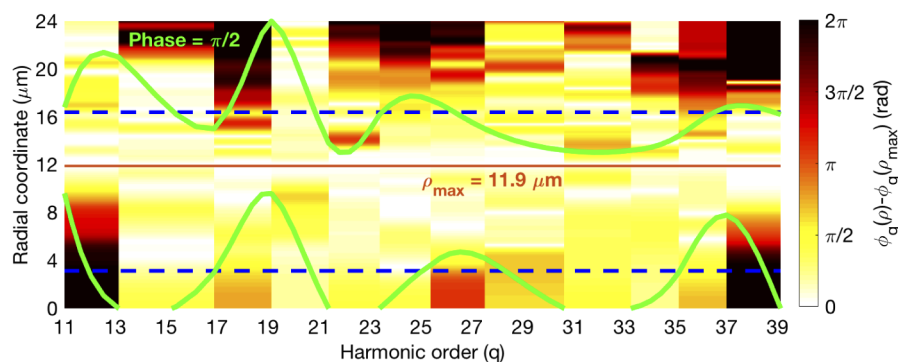

Fig. 5. Relative phase of the harmonics with respect to the emission at ρ_{max} (orange line). The green lines show the boundaries of the phase-matched region around the circle of maximum efficiency, with phase variation less than $\pi/2$ relative to that at $\rho = \rho_{max}$, the average is given by the blue-dashed lines.

of 4 μm (green line) and 12 μm (purple line). These spatial regions are depicted in Fig. 6(b), together with the beam waist of the driving beam (blue-dashed line). While the HHG spectrum of the thin ring differs substantially from that of the whole layer, the thicker one exhibits an excellent agreement. Note that 12 μm thickness is a fair approximation to the phase-matched region identified in Fig. 5.
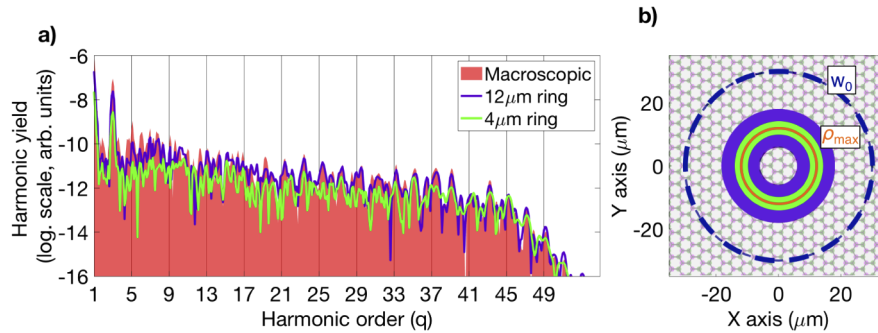

Fig. 6. HHG emission from the phase-matched graphene ring. a) Macroscopic coherent HHG emission resulting from the whole graphene layer (filled-red), and from a ring centered at $\rho = \rho_{max}$ with a thickness of 4 μm (green line) and 12 μm (purple line). These spatial regions at the graphene-layer are depicted in panel b), where the beam waist of the driving beam ($w_0 = 30$ μm) is indicated by the blue-dashed line.

Finally, we note that the fact that all the harmonics are generated from the same annular region in the graphene layer, implies that the far-field divergence of the harmonics decreases with the harmonic order. This result, that is a consequence of the diffraction of a ring structure with progressive shorter wavelength, was already observed in the results presented in Fig. 2(b).

4. Conclusion

We present a theoretical method to compute both microscopic and macroscopic HHG in solids, similar to what has been used in atomic or molecular targets. We have applied this model to calculate HHG in a two-dimensional layer of graphene, evidencing the connection between the microscopic an macroscopic physics of HHG. On one hand, we observe that the macroscopic HHG spectrum presents cleaner harmonic peaks, as it has been observed in different experiments of HHG in solids. On the other hand, the analysis of the macroscopic HHG emission allows to characterize the non-perturbative dynamics of the microscopic emission, such as the power scaling law. Most interestingly, we show that the macroscopic high-order harmonic emission is dominated by an annular region at the target, with radius approximately constant with the harmonic order. We demonstrate that this finding is a direct consequence of the non-perturbative scaling of the microscopic HHG. Our results show the relevance of considering transverse phase-matching even in 2D solids, when irradiated with intense driving fields. Our work opens the route to study macroscopic effects of HHG in other Dirac-Weyl materials, and in more complex macroscopic geometries. For example, it paves the way in the emerging field of structured laser beams with custom angular momentum properties when considering HHG in solid targets. In such scenarios the macroscopic description of the HHG process is absolutely needed to unveil the up-conversion rules of the angular momentum properties.

Disclosures. The authors declare no conflicts of interest.

References

1. A. McPherson, G. Gibson, H. Jara, U. Johann, T. S. Luk, I. A. McIntyre, K. Boyer, and C. K. Rhodes, "Studies of multiphoton production of vacuum-ultraviolet radiation in the rare gases," J. Opt. Soc. Am. B **4**(4), 595–601 (1987).
2. M. Ferray, A. L'Huillier, X. F. Li, L. A. Lompre, G. Mainfray, and C. Manus, "Multiple-harmonic conversion of 1064 nm radiation in rare gases," J. Phys. B: At., Mol. Opt. Phys. **21**(3), L31–L35 (1988).
3. T. Popmintchev, M. C. Chen, D. Popmintchev, P. Arpin, S. Brown, S. Alisauskas, G. Andriukaitis, T. Balciunas, O. Mücke, A. Pugzlys, A. Baltuska, B. Shim, S. E. Schrauth, A. Gaeta, C. Hernández-García, L. Plaja, A. Becker, A. Jaron-Becker, M. M. Murnane, and H. C. Kapteyn, "Bright coherent ultrahigh harmonics in the keV x-ray regime from mid-infrared femtosecond lasers," Science **336**(6086), 1287–1291 (2012).
4. F. Krausz and M. Ivanov, "Attosecond physics," Rev. Mod. Phys. **81**(1), 163–234 (2009).
5. L. Plaja, R. Torres, and A. Zaïr, "Attosecond Physics," in *Attosecond Measurements and Control of Physical Systems* (Springer-Verlag, 2013).
6. S. Ghimire, A. D. DiChiara, E. Sistrunk, P. Agostini, L. F. DiMauro, and D. A. Reis, "Observation of high-order harmonic generation in a bulk crystal," Nat. Phys. **7**(2), 138–141 (2011).
7. K. J. Schafer, B. Yang, L. F. DiMauro, and K. C. Kulander, "Above threshold ionization beyond the high harmonic cutoff," Phys. Rev. Lett. **70**(11), 1599–1602 (1993).
8. G. Ndabashimiye, S. Ghimire, M. Wu, D. A. Browne, K. J. Schafer, M. B. Gaarde, and D. A. Reis, "Solid-state harmonics beyond the atomic limit," Nature **534**(7608), 520–523 (2016).
9. G. Vampa, C. R. McDonald, G. Orlando, D. D. Klug, P. B. Corkum, and T. Brabec, "Theoretical analysis of high harmonic generation in solids," Phys. Rev. Lett. **113**(7), 073901 (2014).
10. H. Liu, Y. Li, Y. S. You, S. Ghimire, T. F. Heinz, and D. A. Reis, "High-harmonic generation from an atomically thin semiconductor," Nat. Phys. **13**(3), 262–265 (2017).
11. A. A. Lanin, E. A. Stepanov, A. B. Fedotov, and A. M. Zheltikov, "Mapping the electron band structure by intraband high-harmonic generation in solids," Optica **4**(5), 516–519 (2017).
12. O. Schubert, M. Hohenleutner, F. Langer, B. Urbanek, C. Lange, U. Huttner, D. Golde, T. Meier, M. Kira, S. W. Koch, and R. Huber, "Sub-cycle control of terahertz high-harmonic generation by dynamical Bloch oscillations," Nat. Photonics **8**(2), 119–123 (2014).
13. T. T. Luu, M. Garg, S. Yu. Kruchinin, A. Moulet, M. Th. Hassan, and E. Goulielmakis, "Extreme ultraviolet high-harmonic spectroscopy of solids," Nature **521**(7553), 498–502 (2015).
14. M. Hohenleutner, F. Langer, O. Schubert, M. Knorr, U. Huttner, S. W. Koch, M. Kira, and R. Huber, "Real-time observation of interfering crystal electrons in high-harmonic generation," Nature **523**(7562), 572–575 (2015).
15. N. Yoshikawa, T. Tamaya, and K. Tanaka, "High-harmonic generation in graphene enhanced by elliptically polarized light excitation," Science **356**(6339), 736–738 (2017).
16. O. Zurrón, A. Picón, and L. Plaja, "Theory of high-order harmonic generation for gapless graphene," New J. Phys. **20**(5), 053033 (2018).
17. O. Zurrón-Cifuentes, R. Boyero-García, C. Hernández-García, A. Picón, and L. Plaja, "Optical anisotropy of non-perturbative high-order harmonic generation in gapless graphene," Opt. Express **27**(5), 7776–7786 (2019).
18. Z. Y. Chen and R. Qin, "Circularly polarized extreme ultraviolet high harmonic generation in graphene," Opt. Express **27**(3), 3761–3770 (2019).
19. Y. S. You, M. Wu, Y. Yin, A. Chew, X. Ren, S. Gholam-Mirzaei, D. A. Browne, M. Chini, Z. Chang, K. J. Schafer, M. B. Gaarde, and S. Ghimire, "Laser waveform control of extreme ultraviolet high harmonics from solids," Opt. Lett. **42**(9), 1816–1819 (2017).
20. M. Wu, S. Ghimire, D. A. Reis, K. J. Schafer, and M. B. Gaarde, "High-harmonic generation from Bloch electrons in solids," Phys. Rev. A **91**(4), 043839 (2015).
21. T. Higuchi, M. I. Stockman, and P. Hommelhoff, "Strong-field perspective on high-harmonic radiation from Bulk Solids," Phys. Rev. Lett. **113**(21), 213901 (2014).
22. P. G. Hawkins, M. Y. Ivanov, and V. S. Yakovlev, "Effect of multiple conduction bands on high-harmonic emission from dielectrics," Phys. Rev. A **91**(1), 013405 (2015).
23. M. Wu, D. A. Browne, K. J. Schafer, and M. B. Gaarde, "Multilevel perspective on high-order harmonic generation in solids," Phys. Rev. A **94**(6), 063403 (2016).
24. T. T. Luu and H. J. Wörner, "High-order harmonic generation in solids: A unifying approach," Phys. Rev. B **94**(11), 115164 (2016).
25. N. Tancogne-Dejean, O. D. Mücke, F. X. Kärtner, and A. Rubio, "Impact of the electronic band structure in high-harmonic generation spectra of solids," Phys. Rev. Lett. **118**(8), 087403 (2017).
26. P. Salières, A. L'Huillier, and M. Lewenstein, "Coherence control of high-order harmonics," Phys. Rev. Lett. **74**(19), 3776–3779 (1995).
27. P. Balcou, P. Salières, A. L'Huillier, and M. Lewenstein, "Generalized phase-matching conditions for high harmonics: The role of field-gradient forces," Phys. Rev. A **55**(4), 3204–3210 (1997).

28. A. Rundquist, C. G. Durfee III, Z. Chang, C. Herne, S. Backus, M. M. Murnane, and H. C. Kapteyn, "Phase-matched generation of coherent soft x-rays," Science **280**(5368), 1412–1415 (1998).

29. C. G. Durfee III, A. Rundquist, S. Backus, C. Herne, M. M. Murnane, and H. C. Kapteyn, "Phase matching of high-order harmonics in hollow waveguides," Phys. Rev. Lett. **83**(11), 2187–2190 (1999).

30. M. B. Gaarde, J. L. Tate, and K. J. Schafer, "Macroscopic aspects of attosecond pulse generation," J. Phys. B: At., Mol. Opt. Phys. **41**(13), 132001 (2008).

31. T. Popmintchev, M. C. Chen, P. Arpin, M. M. Murnane, and H. C. Kapteyn, "The attosecond nonlinear optics of bright coherent x-ray generation," Nat. Photonics **4**(12), 822–832 (2010).

32. C. Hernández-García and L. Plaja, "Off-axis compensation of attosecond pulse chirp," J. Phys. B: At., Mol. Opt. Phys. **45**(7), 074021 (2012).

33. C. Hernández-García, T. Popmintchev, M. M. Murnane, H. C. Kapteyn, L. Plaja, A. Becker, and A. Jaron-Becker, "Group velocity matching in high-order harmonic generation driven by mid-infrared lasers," New J. Phys. **18**(7), 073031 (2016).

34. I. P. Christov, M. M. Murnane, and H. C. Kapteyn, "Generation and propagation of attosecond x-ray pulses in gaseous media," Phys. Rev. A **57**(4), R2285–R2288 (1998).

35. E. Priori, G. Cerullo, M. Nisoli, S. Stagira, S. De Silvestri, P. Villoresi, L. Poletto, P. Ceccherini, C. Altucci, R. Bruzzese, and C. de Lisio, "Nonadiabatic three-dimensional model of high-order harmonic generation in the few-optical-cycle regime," Phys. Rev. A **61**(6), 063801 (2000).

36. M. Geissler, G. Tempea, and T. Brabec, "Phase-matched high-order harmonic generation in the nonadiabatic limit," Phys. Rev. A **62**(3), 033817 (2000).

37. M. B. Gaarde and K. J. Schafer, "Space-Time Considerations in the Phase Locking of High Harmonics," Phys. Rev. Lett. **89**(21), 213901 (2002).

38. V. Tosa, H. T. Kim, I. J. Kim, and C. H. Nam, "High-order harmonic generation by chirped and self-guided femtosecond laser pulses. I. Spatial and spectral analysis," Phys. Rev. A **71**(6), 063807 (2005).

39. V. S. Yakovlev, M. Ivanov, and F. Krausz, "Enhanced phase-matching for generation of soft X-ray harmonics and attosecond pulses in atomic gases," Opt. Express **15**(23), 15351–15364 (2007).

40. C. Jin, A.-T. Le, and C. D. Lin, "Retrieval of target photorecombination cross sections from high-order harmonics generated in a macroscopic medium," Phys. Rev. A **79**(5), 053413 (2009).

41. C. Hernández-García, J. A. Pérez-Hernández, J. Ramos, E. Conejero Jarque, L. Roso, and L. Plaja, "High-order harmonic propagation in gases within the discrete dipole approximation," Phys. Rev. A **82**(3), 033432 (2010).

42. M. C. Kohler and K. Z. Hatsagortsyan, "Macroscopic aspects of relativistic x-ray-assisted high-order-harmonic generation," Phys. Rev. A **85**(2), 023819 (2012).

43. V. V. Strelkov, V. T. Platonenko, A. F. Sterzhantov, and M. Yu. Ryabikin, "Attosecond electromagnetic pulses: generation, measurement, and application. Generation of high-order harmonics of an intense laser field for attosecond pulse production," Phys.-Usp. **59**(5), 425–445 (2016).

44. M.-C. Chen, C. Mancuso, C. Hernández-García, F. Dollar, B. Galloway, D. Popmintchev, P. C. Huang, B. Walker, L. Plaja, A. A. Jaroń-Becker, A. Becker, M. M. Murnane, H. C. Kapteyn, and T. Popmintchev, "Generation of bright isolated attosecond soft X-ray pulses driven by multicycle midinfrared lasers," Proc. Natl. Acad. Sci. USA **111**(23), E2361–E2367 (2014).

45. C. Hernández-García, T. Popmintchev, M. M. Murnane, H. C. Kapteyn, L. Plaja, A. Becker, and A. Jaron-Becker, "Isolated broadband attosecond pulse generation with near- and mid-infrared driver pulses via time-gated phase matching," Opt. Express **25**(10), 11855–11866 (2017).

46. D. Hickstein, F. Dollar, P. Grychtol, J. Ellis, R. Knut, C. Hernández-García, D. Zusin, C. Gentry, J. M. Shaw, T. Fan, K. Dorney, A. Becker, A. Jaron-Becker, M. M. Murnane, H. C. Kapteyn, and C. G. Durfee, "Non-collinear generation of angularly isolated circularly polarized high harmonics," Nat. Photonics **9**(11), 743–750 (2015).

47. P. C. Huang, C. Hernández-García, J. T Huang, P. Y. Huang, C. H. Lu, L. Rego, D. Hickstein, J. Ellis, A. Jaron-Becker, A. Becker, S. D. Yang, C. Durfee, L. Plaja, H. Kapteyn, M. Murnane, A. Kung, and M. C. Chen, "Polarization control of isolated high-harmonic pulses," Nat. Photonics **12**(6), 349–354 (2018).

48. L. Quintard, V. Strelkov, J. Vabek, O. Hort, A. Dubrouil, D. Descamps, F. Burgy, C. Péjot, E. Mével, F. Catoire, and E. Constant, "Optics-less focusing of XUV high-order harmonics," Sci. Adv. **5**(4), eaau7175 (2019).

49. H. Wikmark, C. Guo, J. Vogelsang, P. W. Smorenburg, H. Coudert-Alteirac, J. Lahl, J. Peschel, P. Rudawski, H. Dacasa, S. Carlstrom, S. Macloa, M. B. Gaarde, P. Johnsson, C. L. Arnold, and A. L'Huillier, "Spatiotemporal coupling of attosecond pulses," Proc. Natl. Acad. Sci. U. S. A. **116**(11), 4779–4787 (2019).

50. C. Hernández-García, J. San Román, L. Plaja, and A. Picón, "Quantum-path signatures in attosecond helical beams driven by optical vortices," New J. Phys. **17**(9), 093029 (2015).

51. K. M. Dorney, L. Rego, N. J. Brooks, J. San Román, C. T. Liao, J. L. Ellis, D. Zusin, C. Gentry, Q. L. Nguyen, J. M. Shaw, A. Picón, L. Plaja, H. C. Kapteyn, M. M. Murnane, and C. Hernández-García, "Controlling the polarization and vortex charge of attosecond high-harmonic beams via simultaneous spin-orbit momentum conservation," Nat. Photonics **13**(2), 123–130 (2019).

52. L. Rego, K. M. Dorney, N. J. Brooks, Q. Nguyen, C. T. Liao, J. San Román, D. E. Couch, A. Liu, E. Pisanty, M. Lewenstein, L. Plaja, H. C Kapteyn, M. M. Murnane, and C. Hernández-García, "Generation of extreme-ultraviolet beams with time-varying orbital angular momentum," Science **364**(6447), eaaw9486 (2019).

53. I. Floss, C. Lemell, G. Wachter, V. Smejkal, S. A. Sato, X. M. Tong, K. Yabana, and J. Burgdörfer, "Ab initio multiscale simulation of high-order harmonic generation in solids," Phys. Rev. A **97**(1), 011401 (2018).

54. C. Hernández-García, I. J. Sola, and L. Plaja, "Signature of the transversal coherence length in high-order harmonic generation," Phys. Rev. A **88**, 043848 (2013).

55. C. Hernández-García, W. Holgado, L. Plaja, B. Alonso, F. Silva, M. Miranda, H. Crespo, and I. J. Sola, "Carrier-envelope-phase insensitivity in high-order harmonic generation driven by few-cycle laser pulses," Opt. Express **23**(16), 21497–21508 (2015).

56. F. Catoire, A. Ferré, O. Hort, A. Dubrouil, L. Quintard, D. Descamps, S. Petit, F. Burgy, E. Mével, Y. Mairesse, and E. Constant, "Complex structure of spatially resolved high-order- harmonic spectra," Phys. Rev. A **94**(6), 063401 (2016).

57. M. Breusing, C. Ropers, and T. Elsaesser, "Ultrafast Carrier Dynamics in Graphite," Phys. Rev. Lett. **102**(8), 086809 (2009).

58. D. Brida, A. Tomadin, C. Manzoni, Y. J. Kim, A. Lombardo, S. Milana, R. R. Nair, K. S. Novoselov, A. C. Ferrari, G. Cerullo, and M. Polini, "Ultrafast collinear scattering and carrier multiplication in graphene," Nat. Commun. **4**(1), 1987 (2013).

59. J. M. Iglesias, M. J. Martín, E. Pascual, and R. Rengel, "Carrier-carrier and carrier-phonon interactions in the dynamics of photoexcited electrons in graphene," J. Phys.: Conf. Ser. **647**, 012003 (2015).

60. L. Rego, C. Hernández-García, A. Picón, and L. Plaja, "Site-specific tunnel-ionization in high harmonic generation in molecules," New J. Phys. **22**(4), 043012 (2020).

61. A. Roberts, D. Cormode, C. Reynolds, T. Newhouse-Illige, B. J. LeRoy, and A. S. Sandhu, "Response of graphene to femtosecond high-intensity laser irradiation," Appl. Phys. Lett. **99**(5), 051912 (2011).

62. A. L'Huillier, Ph. Balcou, S. Candel, K. J. Schafer, and K. C. Kulander, "Calculations of high-order harmonic generation processes in xenon at 1064 nm," Phys. Rev. A **46**(5), 2778–2790 (1992).

63. L. Rego, J. San Román, A. Picón, L. Plaja, and C. Hernández-García, "Nonperturbative twist in the generation of extreme-ultraviolet vortex beams," Phys. Rev. Lett. **117**(16), 163202 (2016).